Multipole method for microstructured optical fibers II: implementation and results

B. T. Kuhlmey[1,2], T.P. White[2], G.Renversez[1], D. Maystre[1], L.C. Botten[3], C. Martijn de Sterke[2], R. C. McPhedran[2]

[1]*Institut Fresnel, Faculté des Sciences et Techniques de Saint Jérôme , 13397 Marseille Cedex 20, France, Unité Mixte de Recherche du CNRS 6133*

[2]*School of Physics, University of Sydney, NSW 2006, Australia*

[3] *School of Mathematical Sciences, University of Technology, Sydney, NSW 2008, Australia*

October 5, 2001

Abstract

We describe the numerical verifications of a multipole formulation for calculating the electromagnetic properties of the modes which propagate in microstructured optical fibers. We illustrate its application to calculating both the real and imaginary parts of the propagation constant. We compare its predictions with the results of recent measurements on a very low-loss microstructured fiber, and investigate the variations in fiber dispersion with geometrical parameters. We also show that the formulation obeys appropriate symmetry rules, and that these may be used to improve computational speed.

1. Introduction

In a previous paper[1], hereafter referred to as I, we presented the development of a multipole formulation for calculating the propagation and field characteristics of microstructured optical fibers (MOF). Here we discuss numerical aspects of the formulation, the choice of its parameters to guarantee accurate results, and its numerical verification. The last is achieved through internal consistency tests, and through a comparison both with other methods[2] and with recent experimental results on a very low loss MOF structure[3]. We also present numerical results illustrating important features of MOF's such as the variation of the geometric loss of the modes which propagate in them and of their dispersion characteristics with MOF parameters. The numerical results given here and in I illustrate some key features of the formulation: incorporation of mode symmetry, so as to answer definitively questions related to modal degeneracy, accurate and sensitive characterization of the geometric loss of modes, ability to deliver other modal data such as dispersion and field profiles, and modest computational requirements.

The description of numerical strategies here is of necessity detailed, since the location of modes requires the finding of an approximate zero of the determinant of a large complex matrix. Such zeros are often difficult to distinguish from false minima at first sight, and it is necessary to employ various validation criteria on the "modes" corresponding to the various putative zeros to identify physically meaningful solutions. It is of course valuable to have numerical or experimental values for similar systems to guide the mode search, and the curves and tables we provide here and in I should provide a comprehensive aid to future workers.

2. Validation and self consistency

The formulation of I requires the finding of modes satisfying a homogeneous equation or field identity of the form

$$\left[\mathbf{I}-\boldsymbol{\mathcal{R}}\left(\tilde{\boldsymbol{\mathcal{H}}}+\tilde{\boldsymbol{\mathcal{J}}}^{\mathrm{B0}}\mathbf{R}^{0}\tilde{\boldsymbol{\mathcal{J}}}^{0\mathrm{B}}\right)\right]\mathcal{B}\equiv\boldsymbol{\mathcal{M}}\mathcal{B}=0. \tag{1}$$

This identity expresses the equality of two sets of field representations: a local expansion in the neighbourhood of each cylindrical inclusion in the MOF

$$E_z=\sum_{m=-M}^{M}\left[A_m^{\mathrm{E}l}J_m(k_\perp^e r_l)+B_m^{\mathrm{E}l}H_m^{(1)}(k_\perp^e r_l)\right]e^{im\theta_l} \tag{2}$$

and a global or Wijngaard expansion

$$E_z=\sum_{l=1}^{N_c}\sum_m B_m^{\mathrm{E}l}H_m^{(1)}(k_\perp^e|\mathbf{r}_l|)e^{im\arg(\mathbf{r}-\mathbf{c}_l)}+\sum_m A_m^{\mathrm{E}0}J_m(k_\perp^e r)e^{im\theta}\ . \tag{3}$$

The Wijngaard expansion is expressed in local coordinates using Graf's addition theorem, truncated to the chosen multipole order M and equated with the local expansion (2). The two expansions for E_z and the corresponding expansions for the scaled magnetic field component K_z only match perfectly for untruncated fields ($M\to\infty$), and so their numerical difference on cylinder surfaces can be used as a powerful indicator of truncation errors and the quality of the matrix null vector location. We illustrate this with an example shown in Figs. 1 and 2 of an air-core MOF. Fig. 1 shows significant field errors occurring around the boundary of the larger central air hole. As well, the low frequency modulation of the field discrepancies indicates some imprecision in the minimization of the determinant. In Fig. 2, the multipole truncation order on the central hole has been increased to $M = 19$, while the truncation order on the smaller holes has been kept at 5. The decrease in field matching errors is evident (note the change in scale in the lower panels between Figs. 1 and 2), as is a slight improvement in the quality of the determinant minimization, manifest as a reduction in the low-frequency modulation. One clear sign of adequate convergence in the formulation is obtained from these comparison plots. When enough terms are included, the error term oscillates like the first neglected term in field expansions (i.e., like $\exp[i(M+1)\theta]$).

A second test of convergence is of course provided by the stability of n_{eff} with respect to increase of M. This is illustrated in Table 1, where we also introduce

$$W = \frac{\int_{C_1} |E_z^{\text{local}}(\theta_1) - E_z^{\text{Wijngaard}}(\theta_1)| d\theta_1}{\int_{C_1} |E_z^{\text{Wijngaard}}(\theta_1)| d\theta_1}. \qquad (4)$$

W is a measure of the accuracy of the equality between the local (2) and Wijngaard expansions (3). With increasing M, W decreases while n_{eff} stabilises, as expected.

We have found that the choice of the truncation parameter M should be made such that this quantity clearly exceeds (by a factor around 1.5) the largest argument of Bessel functions on the boundary of inclusions. This guarantees that the cylindrical functions of largest order in field expansions behave like the cylindrical multipoles of electrostatics to leading order (i.e., like $r^n \exp(im\theta)$ and $r^{-n} \exp(im\theta)$), and ensures rapid convergence with increasing m. This criterion is manifest in the case of Figs 1 and 2 where many more Bessel terms are necessary for the large central hole than for other, smaller holes.

A powerful way of validating a new formulation is also to compare its results with those of a well-established method. We have already[2] presented a comparison of the results of our method with those of the scalar and vector beam propagation methods, for a MOF fiber having a single ring of inclusions, and with the imaginary part of $n_{\text{eff}} = \beta/k_0$ of order 10^{-5}. We note that we have successfully used our formulation to study the effects of increasing the number of rings of inclusions, pushing the imaginary part of n_{eff} down to around 10^{-11}, before losing accuracy in its determination, by direct means. We discuss an indirect method, capable of reaching lower values of the imaginary part, in Section 5.

As we also included in our software the extension of the present formalism to simulate the diffraction of incident light by the structure, we were able to validate the code thoroughly against results from other, well established, diffraction codes. Comparisons with a fictitious source code[4] and other multipole like codes[5,6] in conical incidence with complex or real permittivities in various geometries gave excellent agreement of at least 8 decimal figures on the radar cross section, validating each part of the code separately as well as in its entirety.

3. Symmetry

The incorporation of field symmetry in the multipole formulation has two benefits. Firstly, it enables definitive statements to be made about the degeneracy of modes, even in the presence of the accidental degeneracies which arise when normally distinct modal trajectories cross each other. Secondly, it greatly reduces computational burdens, enabling accurate answers for quite large MOF structures to be obtained rapidly on PC's.

In applying the multipole formulation to large six-fold symmetric MOF's, it is highly advantageous to exploit the symmetry properties in Fig. 3 of I to reduce the size of the matrix $\boldsymbol{\mathcal{M}}$. This can be achieved since only multipole coefficients for inclusions lying in the minimum sector indicated in Fig. 3 of I need be specified; those for holes outside the minimum sector can be obtained by multiplying by the appropriate geometric phase factor (related to $\exp(2\pi i/6)$). The resulting reduction in the order of the matrix $\boldsymbol{\mathcal{M}}$ depends on the type of the mode, being maximal for the non-degenerate modes in Fig. 3 of I, and still being around 3.5 for degenate modes, leading to considerable reductions in processing time. See Appendix A for further details.

A. Implementation

We here discuss the implementation of our method to find modes and dispersion characteristics of a given fibre structure.

1. Finding modes

For this task we need an algorithm aimed at finding all the zeros of the determinant of $\boldsymbol{\mathcal{M}}$ in a region of the complex n_{eff} plane. The algorithm should be economical in function calls as each evaluation of the determinant is computationally very expensive for large structures. As shown in Fig. 2 of I, the zeros are very sharp, so that a very accurate first estimate of the zero is necessary for most simple root-finding routines. More specific algorithms for finding zeros of analytic or meromorphic functions[7,8] have good convergence for simple structures (with six cylinders for example) but fail for more complex structures, even with good initial guesses. Our present approach to root finding seems computationally efficient. We first compute a map of the modulus of the determinant over the region of interest, and then use the local minima of this map as initial points for a mixed zooming and modified Broyden[9] algorithm (an iterative minimization algorithm, guaranteed to converge for parabolic minima). Further details of this method are given in Appendix B.

The initial scanning region has to be chosen in accordance with the physical problem studied: if the fibre is air cored and air guided modes are sought, we choose $\Re(n_{\rm eff}) < 1$, whereas if the fibre has a solid core we usually choose to search for modes in a region where $\Re(n_{\rm eff})$ is between the optical indices of the inclusions and the matrix. In the latter case hundreds of modes may exist for small $\Re(n_{\rm eff})$ which are of little interest because of their high losses. We therefore often concentrate on a smaller $n_{\rm eff}$ scanning region near the highest index of the structure. A scanning region for $\Im(n_{\rm eff})$ giving good results in almost any case is $10^{-12} < \Im(n_{\rm eff}) < 10^{-3}$.

2. Dispersion characteristics

The above process of finding modes is carried out for a specific wavelength. We could reiterate the search for modes for many different wavelengths to obtain dispersion characteristics, but this process would be quite laborious. We have found two alternative methods to be of value. One computes and identifies the modes for three or four different wavelengths, then uses a spline interpolation to estimate the $n_{\rm eff}$ values for other wavelengths and refines the estimate with the mixed zooming and Broyden algorithm. Each newly determined point of the $n_{\rm eff}(\lambda)$ curve can be used to enhance the spline estimate. The second (and often more efficient) method is to compute the modes for only one wavelength λ_0, then slightly perturb the wavelength to get $n_{\rm eff}(\lambda_0+\delta_\lambda)$ using $n_{\rm eff}(\lambda_0)$ as a first guess, and then use a first order estimate of $n_{\rm eff}$ at the next wavelength. One can then compute $n_{\rm eff}(\lambda+m\delta_\lambda)$ using a first order estimate computed from the two preceding values. For both methods, the wavelength step has to be chosen very small: For small steps more points are necessary to compute the dispersion characteristics in a given wavelength range, but for large steps the first order guess becomes inaccurate and the convergence of the zooming and Broyden algorithm unacceptably slow. Having small steps and therefore numerous numerical values on the dispersion curve is also of benefit when evaluating second order derivatives, as is necessary to compute the group velocity dispersion.

Material dispersion can be included easily by changing the optical indices according to the current wavelength at each step using, for example, a Sellmeier approximation[10] for silica.

The method described here can be adapted to study the change of $n_{\rm eff}$ of a mode for any continuously varying parameter, for example cylinder radius, cylinder spacing or optical index. One problem that can occur when following the evolution of a mode with a continously varying parameter is mode crossing. This results in wrong data, but can easily be detected in most cases through a discontinuity of derivatives, and can also easily be eliminated by restarting the algorithm with the correct mode on the other side of the crossing.

The correct choice for δ_λ strongly depends on wavelength and structure, so that no general advice can be given. However, as a rough guide, satisfactory results have generally required 200 or more points on curves.

3. Using the symmetry simplifications

When the structure of interest presents symmetries, these can be used to improve considerably the computations, as mentioned in section 3B of I and detailed in Appendix A. The search for modes changes slightly in this case.

To obtain all the modes we now have to check for each class of modes separately. This implies going through the entire process of evaluating a determinant map and refining each local minimum once per non-degenerate mode class and once for each degenerate pair of mode classes. For a structure with C_{6v} symmetry, six determinant maps have to be evaluated (classes 1, 2, 3, 5, 7 and 8, the modes of classes 4 and 6 being deduced from those of class 3 and 5, *cf.* Fig. 3 of I). But as the matrix size is reduced by a factor ranging from 3.5 to more than 6, and the computations scale as the size of the matrix cubed, the overall efficiency gain of using the symmetries remains high. The gain is even higher when computing dispersion figures for a given mode, as only one symmetry class is then concerned.

4. Software and Computational Demands

We have developed a FORTRAN 90 code to exploit the above considerations. For symmetric structures the suggested optimizations are used and the software can therefore deal, even on PC's, with large structures (modes for fibres with 180 holes have so far been computed on current personal computers). Once the structure has been defined, the software is able to find automatically all the modes within a given region of the complex plane for $n_{\rm eff}$ and can optionally track a mode as a function of wavelength to obtain dispersion characteristics. Material dispersion can be included, if desired.

Computational demands are relatively modest: the complete set of modes with $M=5$ in the region of interest $1.4 < \Re(n_{\rm eff}) < 1.45$ for the structure used in Fig. 2 of I and Fig. 4 – 6 of I can be computed on a current

Pentium III (733MHz) personal computer in less than 3 minutes using less than 2Mb of memory. Of course the load rises for larger structures, but the complete set of modes for a structure of three layers of holes in a hexagonal arrangement as used in section 4 B of this paper takes less than an hour (and about 15Mb memory) on a Compaq workstation. Dispersion curves can be computationally more expensive: the loss curves in section 4 B took from about half an hour (for $d/\Lambda = 0.075$ where we used $M = 5$) to several hours (for $d/\Lambda = 0.7$ where $M = 7$ was needed for accuracy).

4. Fibre geometry and mode properties

A. Dispersion in MOF's

One of the important features of MOF's is the powerful control their geometry exerts over the dispersion characteristics of modes[11]. In a standard single mode fiber, the total dispersion consists of material and waveguide contributions, whose combination is normal in the near infrared for wavelengths up to $\lambda_{zc} \simeq 1.31\mu$m, and anomalous beyond that[10]. Dispersion shifted fibers can shift the zero dispersion point to longer wavelengths, while dispersion can be reduced over a range of wavelengths by other designs.

In Fig. 3, we show the evolution of key dispersion parameters with both wavelength and hole radius for a solid core MOF with three rings of holes, for which the index of silica is modelled by the Sellmeier equation. The parameters displayed are $\Re(n_{\text{eff}})$, $\Im(n_{\text{eff}})$, v_g/c and D, where

$$v_g = c\left(n_{\text{eff}} + \omega\frac{dn_{\text{eff}}}{d\omega}\right)^{-1} \tag{5}$$

is the group velocity[10], and

$$D = -\frac{\lambda}{c}\frac{d^2\beta}{d\lambda^2} \tag{6}$$

is the dispersion parameter. Noticeable trends in the four quantities are the steady decrease in $\Re(n_{\text{eff}})$ as the hole size increases, the decrease in the loss or $\Im(n_{\text{eff}})$ with increasing hole size and better confinement, the steady increase in group velocity with increasing air fraction, and the movement of λ_{zc} with hole diameter, initially above the step-index fiber value, and then back down through it and sweeping towards the visible as d/Λ increases further. This ability to vary the zero dispersion point by a wavelength factor approaching two offers exciting possibilities for fiber designs[11].

B. Geometrical losses

As modes in MOFs are not strictly confined but lossy, it is important to be able to evaluate the geometrical losses intrinsically related to the MOF geometry. We studied the case of a silica MOF perforated with cylindrical air holes whose centers are arranged hexagonally and computed the loss figures for the first few modes at a wavelength of 1.55μm with varying pitch, diameter to pitch ratio and number of rings. In this study, the jacket was taken to be silica.

Fig. 4 shows the loss figures for the fundamental mode of a solid core MOF with three rings of holes with varying pitch, for different diameter to pitch ratios. It is clear that guidance becomes better for bigger holes, and our simulations show that larger pitches are favorable to lower losses. This can be explained phenomenologically as the real part of the effective index of the fundamental mode tends to the refractive index of silica, so that the propagation is more and more parallel to the fiber axis. Interaction with the confining structure is thus minimized.

This behaviour is also found for non-fundamental modes. Fig. 5 shows the loss figures with varying pitch for the first three modes of a MOF with three rings of holes, for a diameter on pitch ratio of $d/\Lambda = 0.4$. Note that non-fundamental modes always exist, even for structures claimed to be single-mode, but can be much more lossy than the fundamental mode. As losses vary continuously with parameters and no truly bound modes exist in the case of MOFs, the definition of a single mode MOF can only be relative. Moreover, it emerges from our numerical results that introducing an air jacket around the MOF makes these three modes truly bound ($\Im(n_{\text{eff}}) = 0$), while others remain leaky. This phenomenon shows the importance of the jacket, and is currently under investigation.

Data showing confinement loss as a function a function of the number of rings and their diameter to pitch ratio, with $\Lambda = 2.3\mu$m, for a wavelength $\lambda = 1.55\ \mu$m, has been given already[12]. Depending on the value of d/Λ, up to eight rings of holes were necessary to reduce geometrical loss to below 1 dB/m.

5. Theory and Experiment

We compared results from our simulations with experimental data published by Kubota *et al.*[3] The MOF used for their experiments was a silica fiber with approximately 7 rings of air holes disposed in a very regular hexagonal lattice, the core being created by a missing hole (Fig. 6). For our simulations we used the geometrical data as published, but varied the number of rings from one to seven. We used the Sellmeier approximation for the index of silica.

A first result is that there is no need for having a large number of rings to reach geometrical losses of the order of losses of conventional fibers. Fig. 7 shows the loss figures for the first three modes versus the number of rings at a wavelength of 0.76 μ m. These figures only include geometrical losses, absorption or Rayleigh scattering having not been included: they show the limitations due to the confinement by a MOF structure.

With two rings, the fiber has a single-mode behavior for kilometric lengths, as only the fundamental mode propagates without significant losses, but with more than two rings other modes become virtually lossless. This is in agreement with the multi-mode behaviour observed experimentally for seven rings of holes. Clearly, three rings of holes are theoretically enough to ensure a guidance only limited by losses due to absorption or structural imperfections. We confirm that the losses observed by Kubota *et al.* (7.1dB/km at 850 nm) are not due to the limitation imposed by the MOF geometry of the fiber but mainly to Rayleigh scattering, structural imperfections and absorption.

The imaginary parts of $n_{\rm eff}$ corresponding to Fig. 7 are well below those able to be determined directly by determinant minimization. Instead we must proceed through its evaluation by an energy flux argument, once the real part of $n_{\rm eff}$ has been determined to high accuracy by determinant minimization. The loss coefficient α is obtained through the conservation of the time averaged flux of the Poynting vector $\mathbf{S}$ through a cylinder of elementary length δz centered at the origin and with a radius R such that the cylinder includes all inclusions. We have:

$$\iint_{\theta,\rho<R} \Re(\mathbf{S}(\rho,\theta,z)).\mathbf{u_z}\rho d\rho d\theta = \delta z \oint_\theta \Re(\mathbf{S}(R,\theta,z)) .\mathbf{u_r} R d\theta + \iint_{\theta,\rho<R} \Re(\mathbf{S}(\rho,\theta,z+\delta z)).\mathbf{u_z}\rho d\rho d\theta \qquad (7)$$

where $\mathbf{u_z}, \mathbf{u_r}$ are the usual unit vectors of the local basis in cylindrical coordinates. As $\mathbf{S}$ varies as $e^{-\alpha z}$, we have

$$\mathbf{S}(\rho,\theta,z+\delta z) \simeq (1-\alpha\delta z)\mathbf{S}(\rho,\theta,z) \qquad (8)$$

so that (7) becomes

$$\alpha \iint_{\rho<R,\theta} \Re(\mathbf{S}(\rho,\theta,z)).\mathbf{u_z}\rho d\rho d\theta = \oint_\theta \Re(\mathbf{S}(R,\theta,z)).\mathbf{u_r} R d\theta \ . \qquad (9)$$

Isolating α gives

$$\alpha = \frac{\oint_\theta \Re(S_r(R,\theta,z))Rd\theta}{\iint_{\theta,\rho<R} \Re(S_z(\rho,\theta,z))\rho d\rho d\theta} \qquad (10)$$

where we have introduced S_z and S_r, components of $\mathbf{S}$ in cylindrical coordinates. The imaginary part of the effective index is then given by

$$\Im(n_{\rm eff}) = \frac{\alpha}{2k_0} \ . \qquad (11)$$

We computed dispersion figures for the fundamental mode of the Kubota structure. We first observed that the number of rings has very little influence on the actual dispersion curve, as the fundamental mode is already well confined with one ring. We therefore used a one ring structure in subsequent simulations to improve computational speed, without losing significant accuracy for dispersion parameters. Although we observed a shift of the zero dispersion wavelength to the 800 nm band, we did not find an exact agreement with the experimental zero-dispersion wavelength of 810 nm. With the given geometrical data, we found a zero dispersion wavelength of 889 nm. Kubota *et al.* found similar results with an FDTD method. In order to explain the difference with experimental data, we have computed the zero dispersion wavelength for different hole pitch and diameter: Fig. 8 is for varying pitch with constant diameter, Fig. 9 is for varying diameter with constant pitch and Fig. 10 is for varying pitch and diameter with constant pitch/diameter ratio. These figures show that a variation of about 15% in the pitch with constant diameter or 25% in the pitch with constant diameter/pitch ratio is necessary to obtain the experimental zero dispersion wavelength.

6. Conclusions

The accuracy and computational speed of the multipole formulation described above offer important advantages for understanding or exploiting the properties of MOF fibers. The results presented show clearly the detail it can offer on field structures and symmetry properties. It is at present limited to designs composed of non-intersecting circular inclusions, but nevertheless it can be employed in studies ranging over a wide parameter space: hole radius, spacing, number of rings, packing geometry, air or solid core,*etc.* As we saw, the strong index contrast between air and silica means that fiber parameters can be tuned across a wide range as these parameters vary, so that MOF fibers may well offer a new generation of fiber devices with novel properties. Multipole formulations will be a valuable tool in the quest to develop these devices.

One interesting question that merits further investigation is raised in Section 5. The structure of Kubota *et al*[3] was shown to be single-moded for two rings of air holes, and multi-moded for kilometric lengths with three or more rings. The identification of the number of modes which are physically significant at a particular wavelength depends on the fibre length in question, which dictates the upper limit on mode loss, one factor in deciding how many modes can compete to carry energy from one end of the fiber to the other. As we have seen, the mode loss varies strongly with mode number, hole spacing and size, and the number of rings of holes. Thus, a comprehensive numerical study will be necessary to provide data on mode loss as a function of these parameters, from which a useful definition of mode number in MOF's may emerge.

Finally, we add a few remarks placing our multipole method in the context of the range of competing techniques for numerically studying MOF's. As we have shown, the multipole method is capable of yielding the geometric loss of finite MOF confining structures, with $\Im(n_{\text{eff}})$ being accessible down to 10^{-14} or lower. This is a feature not likely to be emulated easily by other methods, and is certainly unique at this time. Secondly, the method has been constructed in such a way that symmetry properties of modes can be enforced within the formulation, so that questions of degeneracy are exactly answered. Thirdly, it delivers highly accurate data on propagation constants and field patterns for modes using quite modest computing resources, if the MOF contains a reasonable number of air holes. There are drawbacks of the method of course: it is at present restricted to circular air holes, and the mode searching for an unfamiliar geometry may be difficult and time consuming. Nevertheless, the multipole formulation is likely to prove highly valuable in coming years, as designers move to exploit the manifold possibilities afforded by a new generation of optical fibers.

This work was supported by the Australian Research Council. It has benefited from travel support provided by the French and Australian Governments. H. Kubota is thanked for discussion of experimental results and provision of figures.

Appendix A: Symmetrization of modes

We consider waveguides with C_{6v} symmetry, such as the structures in Fig. 6. From McIsaac[13], such structures have 8 mode classes, with 4 of these occurring as 2 degenerate pairs, as shown in Fig. 3 of I. For the purpose of this example we are interested in the degenerate fundamental modes $p = 3$ and $p = 4$ and the lowest order non-degenerate modes $p = 1$ and $p = 2$. The minimum waveguide segments illustrated in Fig. 3 of I represent the smallest segment of the fibre required to define fully the modal fields of the complete structure. We relate the multipole coefficients for a secondary cylinder outside the minimum segment to those of the corresponding primary cylinder inside the segment.

From Fig. 3 of I the non-degenerate mode classes 1 and 2 have minimum waveguide segments of $\pi/6$, so 3 primary cylinders are required to describe the 18 hole structure shown in Fig. 12. The holes are labeled as P_S where P is the primary cylinder and S the label given to the secondary cylinder. Hole 1_1 is the primary cylinder 1 and lies in the inner shell, while the other primary cylinders 2_1 and 3_1 lie in the second shell. As they are not degenerate, these modes must exhibit the full 6-fold symmetry of the structure.

In terms of the multipole coefficients of the electric field b_m^E, the relation between those on secondary cylinders to those on primary cylinders can be expressed in the form

$$b_m^{E(P_S)} = b_m^{E(P_1)} e^{im(S-1)\pi/3},$$

and similarly for the magnetic field coefficients.

For the degenerate mode classes 3 and 4, the number of secondary cylinders corresponding to a given primary cylinder depends on the position of the primary cylinder. If the primary cylinder lies on a symmetry axis of the mode, in this case either the x or y axis, then only one other cylinder is related to it. A primary cylinder not on a symmetry axis has 3 associated secondary cylinders. A cylinder positioned at the center of the structure has no secondary cylinders. The related primary and secondary cylinders are shown in Fig. 13.

For classes 3 and 4, the fields are either symmetric or anti-symmetric about the transverse axes. The relation between primary and secondary cylinders is obtained by appropriate combinations of reflections and inversions to give the correct symmetry properties.

For mode $p = 3$, the multipole coefficients on a secondary cylinder lying on the x-axis are related to those on the corresponding primary cylinder by a simple reflection of E_z and anti-reflection of K_z across the y-axis:

$$b_m^{E(P_2)} = -b_{-m}^{E(P_1)}, \quad b_m^{K(P_2)} = b_{-m}^{K(P_1)}.$$

Similarly, for a secondary cylinder on the y-axis, the relations are

$$b_m^{E(P_2)} = (-1)^m b_{-m}^{E(P_1)}, \; b_m^{K(P_2)} = (-1)^{m+1} b_{-m}^{K(P_1)}.$$

As mentioned, a primary cylinder that does not lie on either axis has three associated secondary cylinders. The relations are again combinations of reflections and anti-reflections about the axes:

$$\begin{aligned} b_m^{E(P_2)} &= -b_{-m}^{E(P_1)}, & b_m^{K(P_2)} &= b_{-m}^{K(P_1)}, \\ b_m^{E(P_3)} &= (-1)^{m+1} b_m^{E(P_1)}, & b_m^{K(P_3)} &= (-1)^{m+1} b_m^{K(P_1)}, \\ b_m^{E(P_4)} &= (-1)^m b_{-m}^{E(P_1)}, & b_m^{K(P_4)} &= (-1)^{m+1} b_{-m}^{K(P_1)}. \end{aligned}$$

The relations for the second degenerate mode class $p = 4$ are simply obtained by swapping the b_m^E and b_m^K coefficients in the equations above.

These symmetry relations are used in our method to re-express the field identity (1) in terms of the primary cylinders only. This reduces the matrix dimensions by a factor between 3.5 and 6, depending on the mode class, thus greatly increasing the calculation speed and allowing larger structures to be studied.

Appendix B: Algorithm

We compute the determinant for a number of points $0 \leq i_r \leq N_r$ over $0 \leq i_i \leq N_i$ lines parallel to the real axis, with imaginary parts varying exponentially with i_i. The exponential variation of the imaginary part is necessary as different modes can have losses differing by several orders of magnitude. Local minima of this array are computed through simple data analysis, and better initial guesses of the minima are estimated through interpolation of the points adjacent to each minimum. This guess is used as a starting point for a Broyden-like algorithm. If the algorithm fails, a new map of the determinant is computed over the region in which the first mapping showed there is a local minimum. This refinement map uses a region of 5×5 points, with a linear scale for both real and imaginary parts. If the only minima of the refined region are on its border, the region is extended until a minimum lies inside the region. During the enlargement of the region, care is taken to avoid regions overlapping with regions in which computing errors can occur (negative or excessive imaginary or real part). If a minimum is found in the refined region (excluding the borders), the routine tries the Broyden-like algorithm again. If multiple minima are found in the region, each minimum is added to the initial minima list and is treated separately: missing a zero thus becomes very unlikely. During the Broyden algorithm a calculation of singular values is performed (see Section 3A of I) each time the modulus of the determinant for the current point is less than a parameterized threshold, and the modules of the eigenvalues are analysed to determine whether an acceptable solution has been found (see the discussion in section 3A of I).

The routine continues to alternate Broyden and zooming algorithms until one of the following occurs:

- an acceptable solution is found,
- the extended mapping region concentrates near a border of the initial region,
- the refined region becomes too small,
- the extended mapping region includes a minimum of the initial determinant map which has already been treated,
- a maximum number of iterations is reached.

Depending on the width of the initial scanning region and the complexity of the structure, the pertinent choice of N_r varies from about 50 to several hundreds: structures with a substantial number of cylinders have a higher density of modes and therefore need a better resolution on the initial determinant map. The value of N_i, even for intricate structures, does not need to be high, and is usually taken between 4 and 8: as shown by Fig. 2 of I, zeros are usually associated with valleys parallel to the imaginary axis, so that precise maps parallel to the real axis for a few values of the imaginary part are sufficient to find a first estimate of the zeros.

---

1. T.P. White, B.T. Kuhlmey, R.C. McPhedran, D. Maystre, G. Renversez, C.M. de Sterke and L.C. Botten, “Multipole method for microstructured optical fibers I: Formulation”.
2. M.J. Steel, T. P. White, C.M. de Sterke, R.C. McPhedran, and L.C. Botten, “Symmetry and Degeneracy in Microstructured Optical Fibres”, Optics Letters, **26**, 488-490 (2001).
3. H. Kubota, K. Suzuki, S. Kawanishi, M. Nakazawa, M. Tanaka, M. Fujita, “Low-loss, 2km-long photonic crystal fiber with zero GVD in the near IR suitable for picosecond pulse propagation at the 800 nm band”, in OSA *Trends in Optics and Photonics (TOPS) Vol.56, Conference on Lasers and Electro-Optics (CLEO2001)*, Technical Digest, Postconference Edition (Optical Society of America, Washington DC, 2001), paper CPD-3.
4. F. Zolla, R. Petit,“Method of fictious sources as applied to the electromagnetic diffraction of a plane wave by a grating in conical mounts”, J. Opt. Soc. Am. A, **13**, 1087-1096 (1996).
5. D. Felbacq, G. Tayeb, and D. Maystre, “Scattering by a random set of parallel cylinders,” J. Opt. Soc. Am. A **11**, 2526-2538 (1994).
6. E. Centeno, D. Felbacq, “Rigorous vector diffraction of electromagnetic waves by bidimensional photonic crystals”, J. Opt. Soc. Am. A, **17**, 320-327 (2000).
7. P. Kravanja, M. Van Barel, “Computing the Zeros of Analytic Functions”, (Springer, Berlin, 2000).
8. L. C. Botten, M. S. Craig, R. C. McPhedran, “Complex Zeros of Analytic Functions”, Comp. Phys. Comm., **29**, 245-259 (1983).
9. C. G. Broyden, “A Class of Methods for Solving Nonlinear Simultaneous Equations ”, Mathematics of Computation, **19**, 577-593 (1965).
10. G. P. Agrawal, “Nonlinear fiber optics” (Academic Press, San Diego, 1995).
11. D. Mogilevtsev, T.A. Birks and P. St. J. Russell, “Group-velocity dispersion in photonic crystal fibres”, Opt. Lett. **23**, 1662-1664 (1998).

12. T. P. White, R. C. McPhedran, C.M. de Sterke and M. J. Steel, "Confinement losses in microstructured optical fibres", Opt. Lett. (to appear, 2001).
13. P. R. McIsaac, "Symmetry-induced modal characteristics of uniform waveguides-I: Summary of results", IEEE Trans. Microwave Theory Tech. **MTT-23**, 421-429 (1975).

M	$\Re(n_{\text{eff}})$	$\Im(n_{\text{eff}}) \times 10^6$	W
3	1.43852886240663	6.918242988502046	9.7×10^{-2}
4	1.43838719374803	1.749096334333127	4.6×10^{-2}
5	1.43836672605884	1.373925319699950	1.5×10^{-2}
6	1.43836499998690	1.414928166193201	2.7×10^{-3}
7	1.43836493475660	1.416468499483090	9.3×10^{-4}
8	1.43836493461317	1.416459892560528	7.7×10^{-4}
9	1.43836493424529	1.416475747100788	2.5×10^{-4}

Table 1. Convergence of n_{eff} with M. Results are for the $p = 1$ mode of the MOF in Table 1 of I at $\lambda = 1.45\,\mu$m. Here W from Eq.(4) gives the degree of accuracy of the equality between Wijngaard and local expansions. The integrals are taken over the boundary of cylinder 1 situated at $r = 6.75\mu$m, $\theta = 0$.

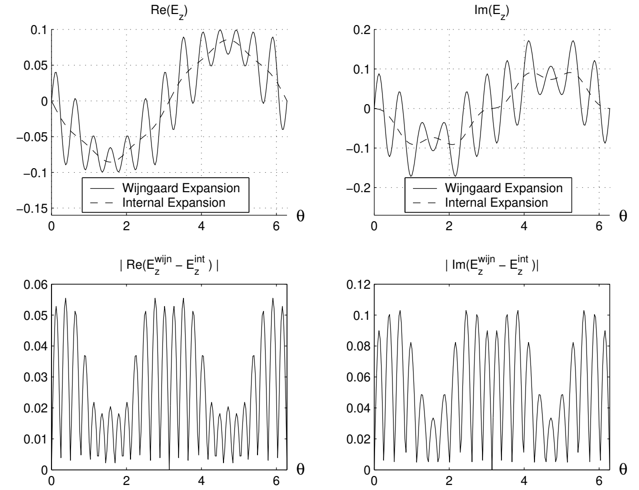

Fig. 1. In the upper and lower parts of the figure, internal and Wijngaard expansions are compared for respectively E_z and K_z, for an air core MOF, with $M = 5$ both for the central air hole and all other air holes (3 rings, 54 air holes of diameter 4.0271 μm, core hole diameter 13.0714 μm, $n_e = 1.39$, $n_i = 1.00$, Λ=5.78157μm, λ=3.846μm.)

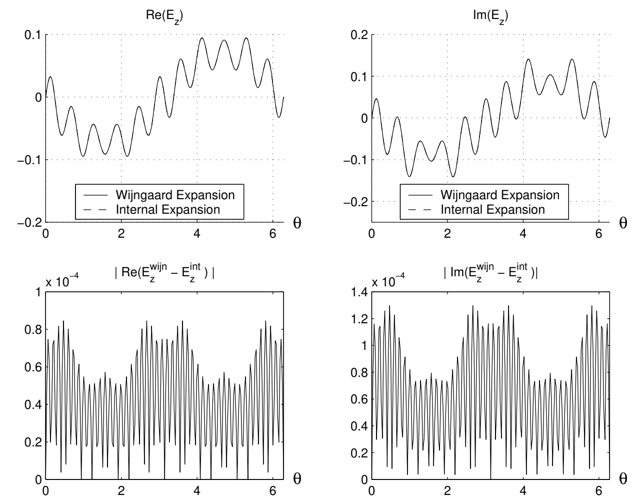

Fig. 2. As for Fig. 1, but with $M = 19$ for the core hole and 5 for all other holes. Note that the Wijngaard and internal expansions now match to graphical accuracy.

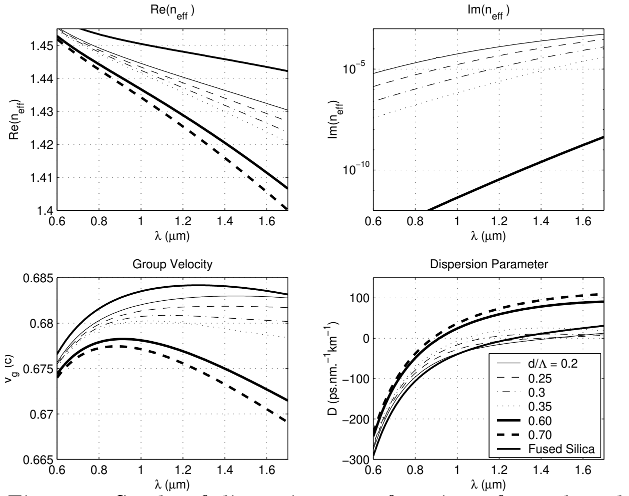

Fig. 3. Study of dispersion as a function of wavelength for solid core MOF's in silica with three rings of holes for various values of d/Λ, with $\Lambda = 2.3\mu$m $n_J = n_{\mathrm{Silica}}$ and Sellmeier model for dispersion of silica.

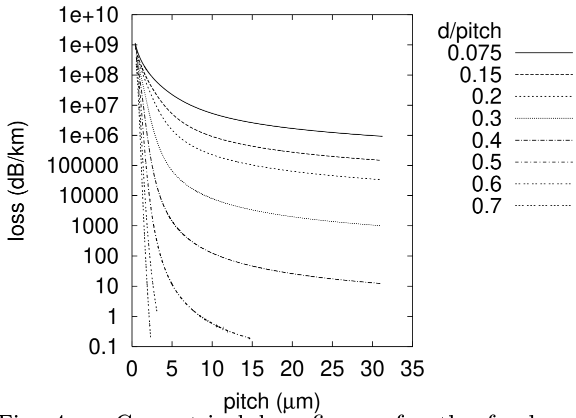

Fig. 4. Geometrical loss figures for the fundamental mode of a MOF with three rings of air holes of varying diameter and pitch. All curves are for $\lambda = 1.55\mu$m.

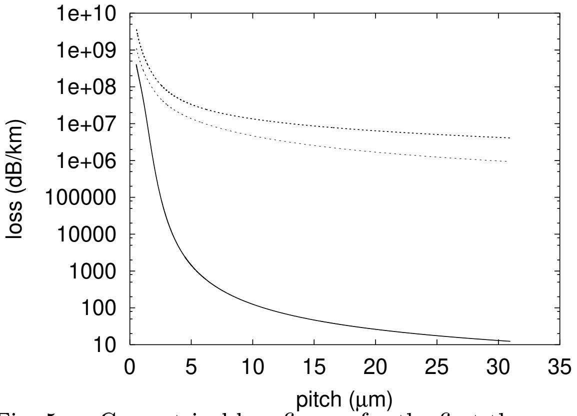

Fig. 5. Geometrical loss figures for the first three modes of a MOF with three rings of air holes as a function of pitch. Here $d/\Lambda = 0.4$, $\lambda = 1.55\mu$m.

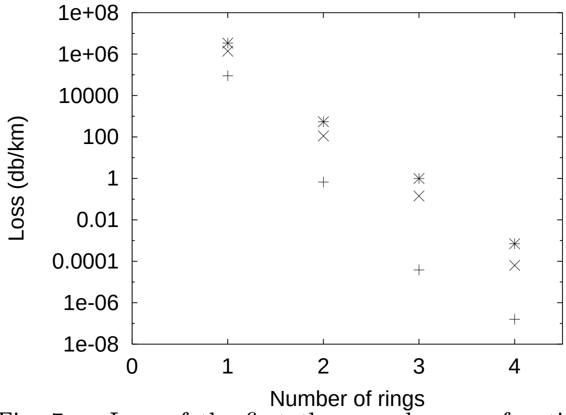

Fig. 7. Loss of the first three modes as a function of number of rings for the structure published by Kubota *et al.*, at a wavelength of 0.76 μm. Only geometrical losses are included.

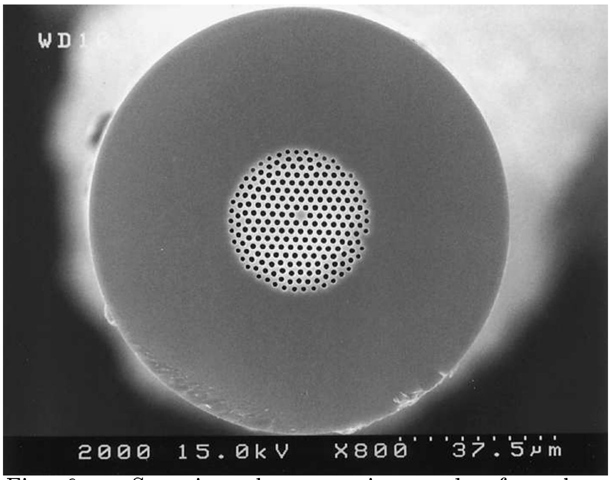

Fig. 6. Scanning electron micrograph of a cleaved end-face of the MOF fabricated by Kubota *et al.* used in our comparisons. Figure supplied by H. Kubota.

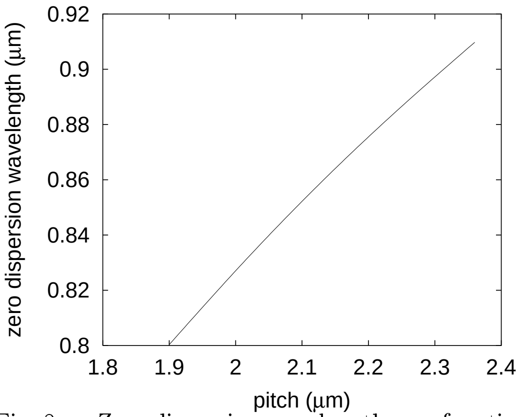

Fig. 8. Zero dispersion wavelength as a function of pitch for the structure published by Kubota *et al.*, with constant diameter $d = 1.51\mu$m.

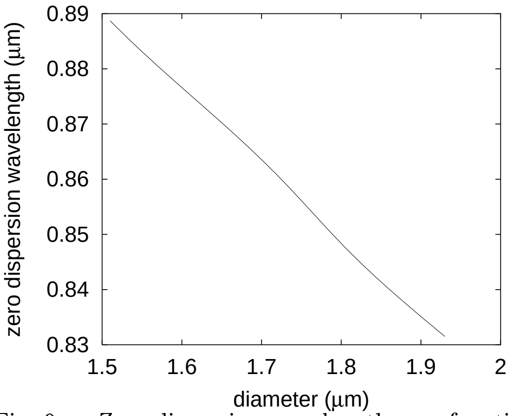

Fig. 9. Zero dispersion wavelength as a function of hole diameter for the structure published by Kubota *et al.*, with constant pitch $\Lambda = 2.26\mu$m.

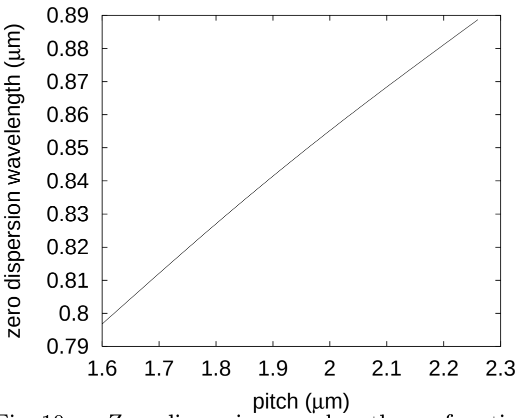

Fig. 10. Zero dispersion wavelength as a function of pitch for the structure published by Kubota *et al.*, with constant diameter/pitch ratio $d/\Lambda = 0.67$.

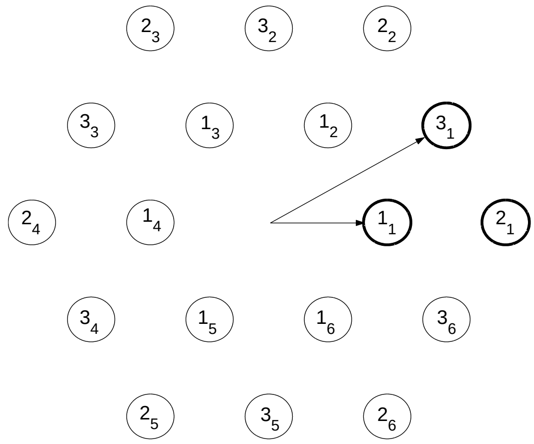

Fig. 11. Primary (bold) and secondary cylinders of the non-degenerate $p = 1$ and $p = 2$ mode classes of a 2-ring MOF structure.

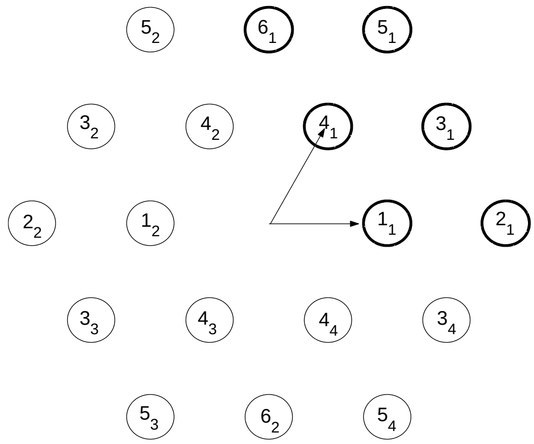

Fig. 12. Primary (bold) and secondary cylinders of the degenerate $p = 3$ and $p = 4$ mode classes of a 2-ring MOF structure.